Composites & nanocomposites

Fabrication, characterization, and gamma ray shielding properties of PVA-based polymer nanocomposite

Nilly A. Kawady[1],* , Mohamed Elkattan[1], M. Salah[2], and Ahmed A. Galhoum[1],*

[1] Nuclear Materials Authority, El-Maadi, P.O. Box 530, Cairo, Egypt
[2] Egyptian Atomic Energy Authority, Cairo 13759, Egypt

ABSTRACT

An innovative cost-effective and lead-free polymer nanocomposite of polyvinyl alcohol/ polyvinyl pyrrolidone was developed. PVA/PVP nanocomposite film contained spherical AgCl and SnO_2 nanoparticles was facilely prepared via a one-pot synthesis method. The synthesis route affords uniform dispersion of the both nanoparticles and unique features of polymer nanocomposite of insoluble, dense, and nonporous properties. The new nanocomposite achieved an efficient gamma radiation attenuation capability. The attenuation capacity for gamma photons was investigated in terms of linear and mass attenuation coefficients (μ) and (μ_m), respectively, at low and high energies (using ^{60}Co and ^{137}Cs sources). Other parameters such as half value layer (HVL), tenth value layer (TVL), and mean free path (MFP) were used to evaluate the shielding capacity. Theoretical calculation (XCOM program) results were consistent with the obtained experimental results. The results revealed that the essential thickness of the polymer nanocomposite to reduce the γ-ray intensity to 50% is 6.6, 8.9, and 9.8 cm for 662, 1173, and 1332 keV γ-ray energies, respectively. The physio-chemical properties of the polymer nanocomposite were evaluated using spectroscopic, microscopic, and thermal analysis tools. Additionally, the formation of spherical nanoparticles was elucidated using TEM. FTIR and leachability were used to confirm the stability, good durability, and chemical resistivity of the synthesized polymer nanocomposite. The nano-filler AgCl and SnO_2 formation mechanism was discussed in detail.

GRAPHICAL ABSTRACT
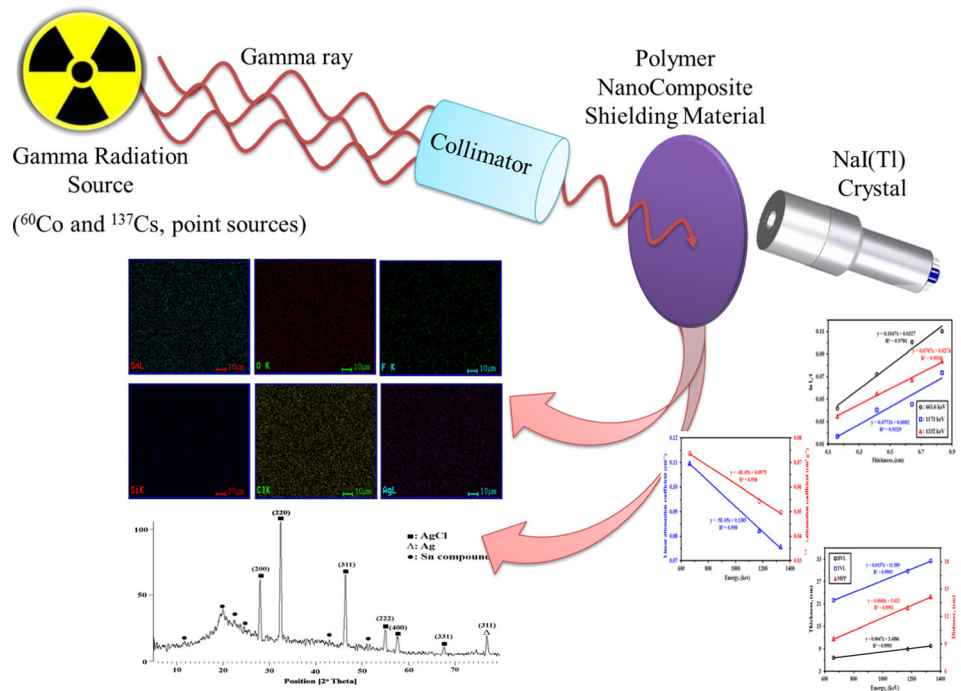
Introduction

Particles of radiant energy, i.e., alpha, beta, neutron particles, and electromagnetic wave emissions, are generated in the form of by-products in a variety of industries, including nuclear power plants, the medical field, and space exploration [1–3]. The electromagnetic (EM) spectrum covers a number of non-ionizing and ionizing radiations with different frequencies between 10^2 and 10^{22} Hz (or 10^8 and 10^{-12} m wavelength) [4]. However, sudden exposures to these radiations may encourage carcinogenesis, mutations of human cells, DNA damage, genetic damage, blood cell damage, and failure of body organs. Consequently, there is always a need to develop new shielding materials that provide efficient protection against radiation hazards [5–7]. Lead can be regarded as the widely foremost material utilized for radiation exposure protection [2, 8]. However, it has a relatively high chemical reactivity with high density and toxicity which make it

environmentally undesirable material [7, 9]. Furthermore, lead high price makes it far from idealized for industrial use and research applications. Therefore, researchers nowadays are interested in finding a lightweight, nontoxic, low-cost, easy-to-be-manufactured materials that could act as a replacement to lead [9, 10]. Lead-free shielding materials provide an appropriate, economical, and environmentally friendly alternative to conventional lead shielding and lead composite materials [9, 11]. Generally, materials have both highly atomic number and density with a good stopping power providing high attenuation efficiency [8, 12]. For example, tungsten is a non-toxic element with density and atomic number approximately high and exhibits better shielding properties with small thickness and a smaller half value layer compared to lead. Even so, purified tungsten has a high cost [9, 13, 14].

On the other hand, nontoxic polymer nanocomposite materials (hybrid nanocomposite materials are multiphase materials, for which one or more of its components has nano-sized dimensions [15, 16]) offer

a successful and effective candidate to be used for radiation shielding [8]. They can be fabricated with low cost compared with high price lead. Furthermore, using polymer composites eliminates the environmental hazards associated with lead materials [17, 18]. Therefore, polymer nanocomposites, which are characterized by lightweight, corrosion resistant, flexibility, can become an appropriate candidate for the conventional shielding applications [19, 20]. The polymer matrix composite materials are considered as one of the vibrant materials, owing to their synergistic properties which are not obtainable with the distinct individual components, including light weight, resistance to weather, moisture, corrosion, and microbial organisms [8, 16, 21]. Synthetic polymers e.g., polyvinyl alcohol (PVA) and polyvinyl pyrrolidone (PVP), have been widely used in different applications [22, 23]. They are characterized as an ecofriendly materials which are characterized by high abrasion resistance, flexibility, high molecular weight, well film formation ability, and low cost [3, 16, 21]. Herein, this study focuses on the one-pot synthesis reaction of a new insoluble hybrid polymer nanocomposite in the presence of HF (PVA/PVP film containing $AgCl/SnO_2$ nanoparticles). Structural and functional specifications of the polymer nanocomposite were extensively examined by XRD, SEM–EDX analysis, XPS, Raman spectrometry, TEM, FTIR, and thermal analysis (TGA/DTA/DSC). Moreover, chemical stability and resistivity of the proposed polymer nanocomposite were evaluated. The polymer nanocomposite fabrication basics and the nanofillers AgCl and SnO_2 formation mechanism were discussed in detail. The radiation shielding of γ-rays absorption and attenuation properties (linear (μ) and mass (μ/ρ) attenuation coefficients) were investigated using low and high γ-radiation energies (^{60}Co and ^{137}Cs, point sources) experimentally and also theoretically using XCOM simulation code. Moreover, half value layer (HVL), tenth value layer (TVL), and mean free path (MFP) calculations were evaluated at different gamma energies for selecting the proper thickness of the gamma shielding from fabricated polymer nanocomposite.

Experimental

Materials and techniques

Polyvinyl alcohol (PVA) (M.wt.: 15,000) and hydrofluoric acid (40%) were supplied from Loba Chemie, India. Polyvinyl pyrrolidone (PVP) (M.wt.: 40,000) was purchased from Universal Fine Chemicals PVT. Ltd., USA. Silver nitrate and tin (II) chloride were obtained from Merck specialties private limited, India. Glycerin (99.5%) was obtained from El Gomhouria Co., Egypt, and other chemicals were Prolabo products. Reagents were used as received.

Preparation of hybrid polymer nanocomposite

Nanocomposite polymer film was prepared using the casting method, based on the optimum condition for the polymer composition synthesis [22], that can be modified to be chemically crosslinked as follows: HF (2.0 mL) was added to distilled water (80.8 mL), and then, add a mixture of the polymers (PVA/PVP) at the weight ratio of 60:40 (6 g:4 g) via continuous stirring for convenient time at 80 °C. After the complete dissolving of the polymer mixture, an equivalent volume of glycerol was added. Then, $AgNO_3$ (1.0 g) has been added, followed by adding of $SnCl_2$ (1.0 g). The final solution was poured in a Petri dish and dried for 84 h at 50 °C in the oven. The polymer nanocomposite (PVA/PVP/HF film containing $AgCl/SnO_2$ nanoparticles) was performed into appropriate spherical according to the collimator opening with different thicknesses (0.11, 0.37, 0.59, and 0.79 cm).

Characterization of the fabricated polymer nanocomposite

The X-ray diffraction (XRD) patterns were obtained using a SmartLab X-Ray Diffractometer (RIGAKU:-Japan), with Cu Kα radiation. The thermogravimetric analysis (TGA) characterizations were obtained using SDT-Q600 V20.5 Pouild 15 (TA Instruments, New Castle, DE:USA). Raman spectroscopy was performed at room temperature using SENTERRA Dispersive Raman Microscope (Bruker, Billerica, MA:USA) at a λ: 532 nm. The surface morphology was investigated using the FEI Inspect-S Electron Scanning Microscope w/Cathodoluminescence

System (USA). The nano-structural features were monitored by the transmission electron microscope (TEM, JEM-2100F, JEOL:Japan). X-ray photoelectron spectroscopy XPS was collected on K-Alpha (Thermo Fisher Scientific:USA). Functional groups of the polymer nanocomposite were analyzed by FTIR spectrometer, Nicolet Nexus 870, USA.

To study the chemical stability of the material, Bai et al., [24] described a simple method for studying and testing the organic polymer chemical stability using leaching with comment acidic and alkaline reagents. So, the fabricated polymer nanocomposite was immersed, treated, and leached at different pHs (1–11). Under the experimental conditions: the polymer nanocomposite has mass 0.144/5 g; aqueous solution 10 mL, temperature 26 °C for 24 h; using in common reagents such as HCl, HNO₃, NaOH solutions, and boiled in tap water for 4 h. After that, samples were filtered, extensively washed with deionized water (both raw sample and after the leaching experiments samples), and were kept at 75 °C for 24 h. The weight loss is (wt% = 100 $(m_0 - m_f/m_0)$: where m_0 is the dry mass before treating and m_f is the dry mass after modification. Moreover, for γ-radiation stability: the nanocomposite material was analyzed by FT-IR spectroscopy before and after the radiation exposure.

The technique of Archimedes was applied to define the density of different thicknesses (0.11, 0.37, 0.59, and 0.79 cm) for the fabricated polymer nanocomposite [25]. Xylene was used as a submerging liquid for that purpose, with a precision of just about ± 0.01 g cm^{-3} at room temperature. After the designation of the fabricated polymer weights, the nanocomposite density was calculated (Eq. 2).

$$\rho_{CE} = \frac{A}{A-B} x \rho_L \qquad (1)$$

where ρ_{CE} is the fabricated polymer nanocomposite experimental density, A the weight of the composite in air, B the polymer nanocomposite weight in the xylene solution, ρ_L the xylene solution density. The experiments were duplicated and showed a standard deviation lower than 6%.

Gamma ray shielding measurements

Attenuation coefficients of γ-ray energies of each thickness were measured for ^{137}Cs and ^{60}Co point sources (Table SI1) at 662, 1173, and 1332 keV,

respectively. Bicron NaI (Tl) scintillation detector with crystal 3″ × 3″mm has 7% resolution for ^{173}Cs, efficiency equal 2 at 0.5 MeV and 1.3 at 2 MeV, sealed hermetically by aluminum house with a photomultiplier tube. The detector is connected with Nuclear Enterprises main shaping amplifier (model NE- 4658, Tennelec high-voltage power supply, model TC 952) with HV digital display and digital MCA gain stabilizer (USA), whereas it was preserved by: (i) a cylindrical copper shield (0.6 cm thickness) against induced X-rays, (ii) a chamber of lead bricks against the environmental radiations, and (iii) a lead shield around the detector (G-5) (5 cm thickness). The detector was also linked with multichannel analyzers (Nuclease PCA-8000 computer-based, 8192) with a color graphical display of spectra with high-level operation technical features by using MAESTRO software. A lead collimator was used to achieve an accurate count of the absorbed gamma radiation. All measurements are carried out at room temperature.

Theoretical background for γ-ray shielding measurements

The full details of this section: linear attenuation coefficient (μ), mass attenuation coefficient (μ$_m$), Half value layer (HVL), tenth value layer (TVL), mean free path (MFP), and XCOM calculation are presented in the Supporting Information Section (Section I in details).

Results and discussion

Polymer nanocomposite fabrication basics

A polymer nanocomposite film has been prepared from polyvinyl alcohol/polyvinyl pyrrolidone (PVA/PVP) polymer by blending and chemical cross-linking, followed by embedding with AgCl/SnO₂.F nanoparticles (Fig. 1). Based on the composition PVA/ PVP weight ratio at 60:40 (i.e., molar ratio is: 0.136:0.036 mol, achieving PVA molar ratio ≈3.78 times), PVP theoretically has the potential of inter-chain hydrogen bonding between the PVA-hydroxyl groups on the chains and carbonyl groups on PVP chains which increase the stability of the polymer network [22]. This conclusion finds agreement with the chemical stability test of the proposed polymer nanocomposite that leads to slight weight loss of uncompleted reacted species.
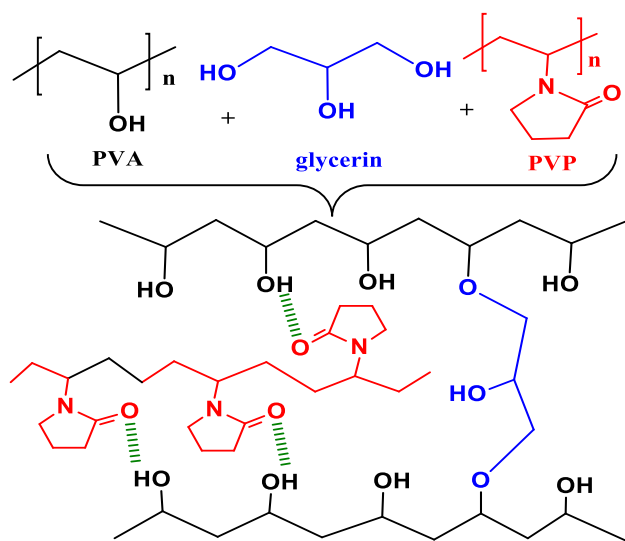
Figure 1 A tentative schematic route for the synthesis of PVP/PVA polymer.

Moreover, adding glycerin could act as a softening agent and a cross-linking agent. The film was formed by a solution casting method. PVA has the film-forming capacity, hydrophilic properties, and a high density of reactive chemical functions that are favorable for cross-linking by irradiation[22], chemical [23], or thermal treatments [26, 27]. Here glycerin and PVP (dipolar imide group) are used as a surfactant, reducing agent, and shape-controlling agent, moreover, as a crosslinking agent (for polyhydroxy PVA polymer) that played an important role in the synthesis process of PVA/PVP/AgCl/SnO$_2$ nanocomposite, since PVP would be beneficial for the adherence between the polymer shell and the inorganic core: where M–O (M: Ag and/or Sn) coordination could be formed through the pyrrolidone ring which was tilted on the Ag surface [28]. While other Ag$^+$ ions have not been reduced yet, as just adding SnCl$_2$, will precipitate as AgCl$_{(s)}$, while oxidation of SnCl$_2$ to SnO$_2$ nanoparticles occurred simultaneously, leading to the formation of the polymer nanocomposite. Besides, PVA/PVP polymer prevents the aggregation of AgCl/SnO$_2$ nanocomposites efficiently.

Addition of SnCl$_2$ to the solution of PAV/PVP/F$^-$/Ag$^+$ can result in formation of AgCl and/or AgF compounds. The formation of AgCl than AgF in this synthesis route can be interpreted according to the HSAB theory (i.e., hard and soft acid base principles, also called Pearson's rules) that reports the preference of soft acids for reacting with soft bases and vice
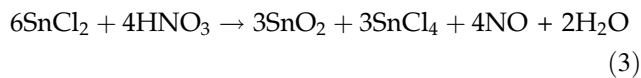
versa [15, 29]. Silver is considered as a soft acid that has a low charge density (high polarizability and electronegativity). Pearson described the interactions of the d-orbital of Ag-atom with the p-orbital of the Cl/F-atom. So, the strong soft acid (Ag$^+$) prefers to associate with the softer base (Cl$^-$:soft/soft nature interaction) compared to (F$^-$:hard/soft interaction)[29], as Cl-atom has larger size with a more diffuse distribution of electrons than F-atom. This also could be predicted by Fajan's rules [30], as the anions increase in size as F$^-$ < Cl$^-$. Since larger ions are more polarizable, covalent character increases and ionic character decreases in the order: AgF < AgCl. This effect increases in the hydration energy and decreases in the lattice energy in the same order [30]. Thus, AgCl should have a higher Δ_{solv} than AgF, yet it is the least soluble in water; the solubility product constant for AgF is (Ksp: 205) while for AgCl (Ksp: 1.8×10^{-10}) [31]. This indicates that AgF is soluble in H$_2$O, but AgCl is not soluble.

Wang et al.[32] described a novel one pot synthesis route of SnO$_2$ nanoparticles using two Sn salts of SnCl$_4$ or SnCl$_2$ as raw materials. The total mole ratio of SnCl$_2$ (or SnCl$_4$):H$_2$O:HAc is (1:150:5). The two kinds of solutions were heated for 15 h at 75 °C to prepare SnO$_2$ precursors and then calcined at different temperatures to obtain SnO$_2$ nanoparticles. Ikhmayies [33] described a simple method to prepare a nanocrystalline fluorine-doped tin oxide (SnO$_2$:F) thin films on glass substrates by dissolving SnCl$_2$ with HF in CH$_3$OH/HCl$_{aq}$. Doping of SnO$_2$ with fluorine to produce SnO$_2$:F was achieved using different fluorine sources: NH$_4$F and/or HF [33, 34].
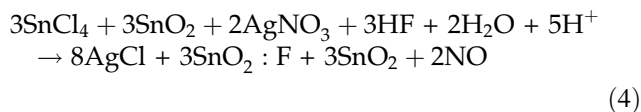
Nano-filler AgCl/SnO$_2$ formation mechanism

The dissolution of AgNO$_3$ (1.0 g $\approx$ 5.89 mmol) has been added into the PVA/PVP/HF solution followed by SnCl$_2$ (1.0 g $\approx$ 5.27 mmol). After complete addition, the synthesized nanocomposite acts as a reducing agent to coordinate and reduces a small portion of Ag$^+$ into Ag$^\circ$ nanoparticles impeded in the polymer composite (before the addition SnCl$_2$). The following mechanism has been proposed as follows (Eqs. 2–4):

$$AgNO_3 + HF \rightarrow AgF + HNO_3 \tag{2}$$

$$6SnCl_2 + 4HNO_3 \rightarrow 3SnO_2 + 3SnCl_4 + 4NO + 2H_2O$$
$$\tag{3}$$

Overall reaction:

$$3SnCl_4 + 3SnO_2 + 2AgNO_3 + 3HF + 2H_2O + 5H^+$$
$$\rightarrow 8AgCl + 3SnO_2 : F + 3SnO_2 + 2NO$$
$$\tag{4}$$

This suggested mechanism was confirmed by the EDX analysis for two areas (Figure SI1) that shows that the films contain (O, Sn, and F) and weight ratios were (47.48:14.61:3.65) and (54.44:16.90:4.34). Thus, the ratio O/Sn in the film is 3.25 and 3.22, respectively, whereas the stoichiometric ratio is 2.0. Here, the ratio is about 3.22–3.25, higher than 2, which is due to the polymer organic portion. Moreover, the Sn:F ratio is 4.00 and 3.89 for areas I and II, respectively, whereas the stoichiometric ratio is 1 in the $SnO_2.F$ nanoparticles. It is noted that the low F (wt%) may be due to the HF initial concentration (limiting reactant), resulting in two types of SnO_2 and $SnO_2.F$. On the other hand, the existence of fluorine atoms may have a role and contribution in the mechanism of polymer formation. This was shown in the EDX analysis (see SEM–EDX section) of the polymer nanocomposite film surface after extensively washed, indicating that the F-atoms were trapped and still present in the polymer film. To the moment, the fluorine role is not clear for us.

Characterization

Crystalline structure-X-ray diffraction pattern

The XRD pattern of the polymer nanocomposite is reported in Fig. 2, which confirmed the nanoparticle composition with a silver crystals and cubic AgCl. Seven characteristic peaks for AgCl cubic phase (JCPDS file: 31–1238) were identified by their khl indices: 200, 220, 311, 222, 400, 331, and 311 diffractions at 2θ: 32.41°, 46.43°, 55.03°, 57.60°, 67.64°, 74.69°, and 76.87° [37]. Obtained peaks are in harmony with the database in the JCPDS file (PDF No. 01–085-1355), which is compatible with the face-centered cubic (FCC) of silver at 76.87° corresponding to (311) hkl plane. This confirms the existence of crystalline Ag/AgCl nanoparticles in the fabricated polymer nanocomposite. Ibarguen et al. [35] explained that the main Sn^{4+} compounds crystalline phases are strongly pH dependent. At low pH, the Sn^{2+} ions may be easily hydrolyzed into polynuclear species; tin, dimmers, and trimmers are possibly produced, e.g., $Sn(OH)^+$, $Sn_2(OH)_2^{2+}$, $Sn_3(OH)_4^{2+}$, although the crystallization of oxides is not very well appear. Moreover, there are other compounds with amorphous forms such as tin chlorides $[SnCl(H_2O)_2$-$SnCl_3(H_2O)]$ at different pHs 1.86, 2.93, 4.50, 6.25, 10.60, respectively. The XRD pattern for the formed compounds at pH 1.86 and 2.93 shows poorly resolved peaks, and the amorphous character

Figure 2 XRD pattern of the polymer nanocomposite film.
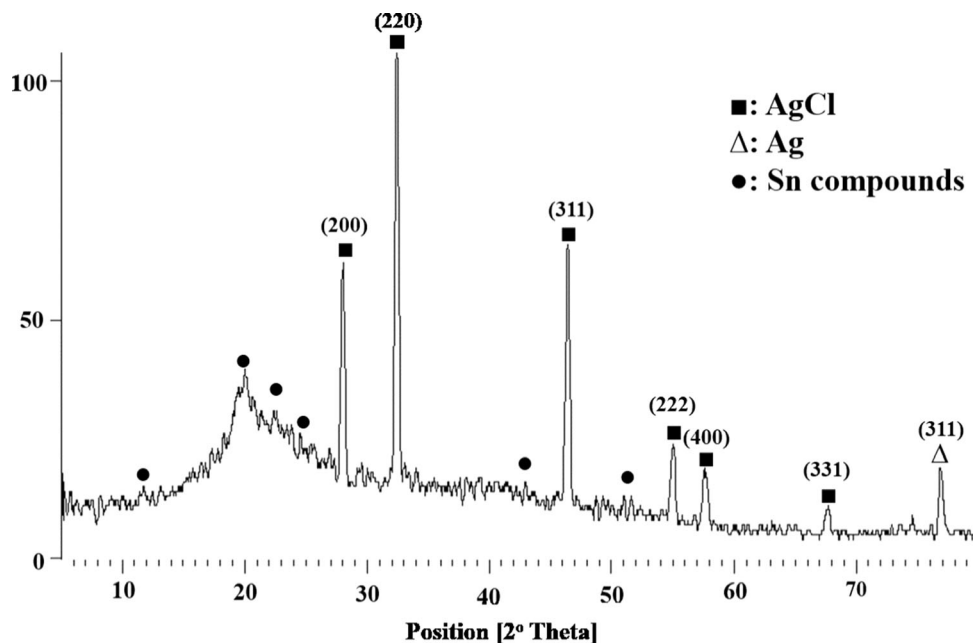
increases with increasing the pHs gradually and tends to disappear completely at pHs 4.50 and 6.25. Using HF during the synthesis process increased the acidity of the composite solution, which can confirm the poor and weak peaks in the ranges (mentioned above). Other peaks may be overlapped with the strong crystallized Ag/AgCl nanoparticles. Moreover, the wide broad peak at $2\theta \approx 20°$ exhibited amorphous nature of the PVA/PVP polymer that is in accordance with that reported before.

SEM–EDX-mapping analysis

The scanning electron microscope was utilized to characterize the morphological structure of the synthesized polymer nanocomposite (Figure SI1). Herein, the polymer film surface can be described as a soft and smooth planar structure with no porosity which is related to the almost dense structure of the polymers PVA/PVP casting composite film and its hydrophilicity, indicating that the use of HF during polymer composite preparation does not activate an etching of the doped inorganic components of Ag and Sn compounds.

Figure SI1 shows EDX mapping analysis for two different areas exhibits the appearance of Ag, Sn, Cl, O, F, and Si signals on the polymer surface with the great homogenous distribution. The specific peak of Sn element was characterized by $L_{\alpha1}$ and $L_{\beta2}$, their peaks being at 3.435, 3.444, and 3.905 keV, respectively, whereas the appearance of the $K_{\alpha1,2}$ and $L_{\beta1}$ distinguished Cl with signals at 2.308, 2621, and 2.816 keV, respectively. The characteristic $L_{\alpha1}$ and $L_{\beta1}$ peaks for Ag were exhibited at 2.984 and 3.151 keV. On the other hand, the occurrence of a tiny peak (poor sensitivity) for Si K_{α} signal was achieved at 1.740 keV. The peaks below 1.0 keV were appeared, especially for O $k\alpha_{1,2}$ and F $k\alpha$ at energies 0.525 and 0.677 keV, respectively. The existence of Si is probably due to impurities contained in the HF or reagents. Results of this analysis confirm the successful preparation of the polymer nanocomposite.

TEM analysis

Figure 3 displays the TEM micrographs of fabricated polymer nanocomposite. The AgCl and SnO_2 nanoparticles have appeared as a spherical dense dots (surrounded by bright areas representing the polymeric shell, due to the difference of electron-

absorbing differences between organic/inorganic components [16, 36]): with a regular spherical structure, well proportioned, and apparently mono-dispersed. This confirms the successful incorporation of nanoparticle into the polymeric matrix. The particle size observed on the TEM images was used to visualize the actual size of the nanoparticles (NPs) and the average particle size found to be 11.4 ± 2.2 nm for AgCl NPs with a narrow particle size distribution. However, in SnO_2 NPs the average particle size is of 26 ± 7 nm with a broad particle size distribution using histograms counting (Figure SI2). This reveals that some Sn-particles tend to aggregate, and this can be attributed to the existence of dipole/dipole attraction force.

Raman analysis

The Raman spectra were recorded as a complementary technique to XRD in order to evaluate the short-range structural order. Figure SI3 shows that two modes located at 68.8 and 238 cm^{-1} were related to the Ag lattice vibrational modes and the stretching of the Ag–Cl bonds located at the terminal positions, respectively [37]. Assis et al. reported that for AgCl, three Raman modes appeared at 60, 147, and 236 cm^{-1} were observed [37]. The existence of SnO_x (x:1 and/or 2) with poorly resolved peaks was detected at 103 and 134 cm^{-1} [38], and unidentified additional peaks with a low intensity (in the region 300–750 cm^{-1}) at 322, 398, 456, 609, and 632 cm^{-1} wavenumbers were detected. For the organic polymer part: numerous bands were observed [39]: (a) broadband 3512 cm^{-1} is assigned to water molecules, (b) broadband between 2936 cm^{-1}, which is specified to a series of asymmetric C–H stretching vibrations, (c) three sharp peaks at 1767, 1637, 1551 cm^{-1} (C = O stretching), 1412 cm^{-1} (CH_3 deformation bend), 1180 cm^{-1} (C–O–C bridge asymmetric stretching), 1091 cm^{-1} (C–C stretching), 992 cm^{-1} (C-N bending), 891 cm^{-1} (C–C stretching), and 809 cm^{-1} (H-bending band) [39].

XPS analysis

Figure 4 illustrates the XPS core level spectra for major elements of polymer nanocomposite. The existence of typical peak of Sn and Cl confirms the successful nanocomposite preparation. The incorporation of AgCl/SnO_2 nanoparticles was occupied the

Figure 3 TEM image **a** low-magnification and **b** higher-magnification visualizing the particle size distribution of both nanoparticles inside the polymer matrix—histogram size distribution.
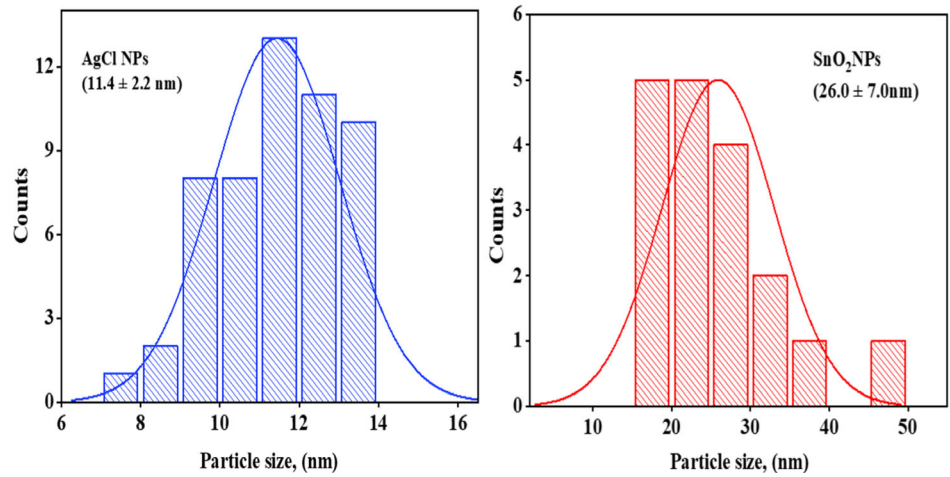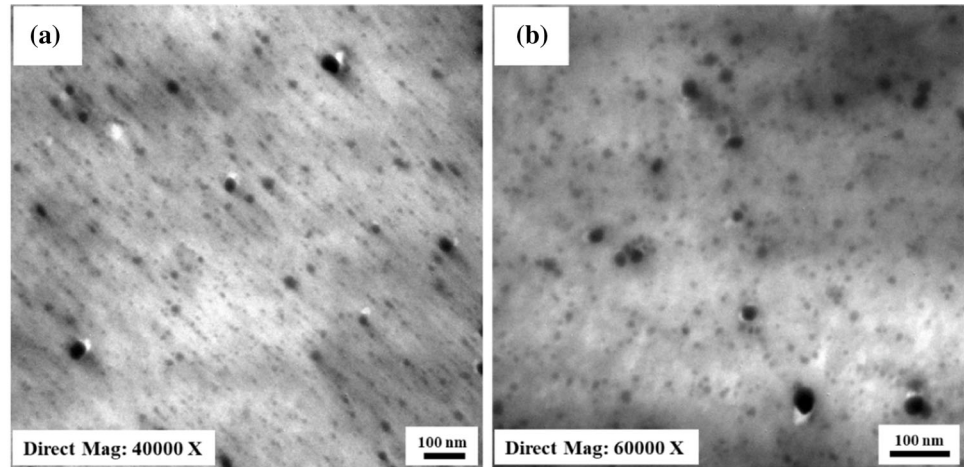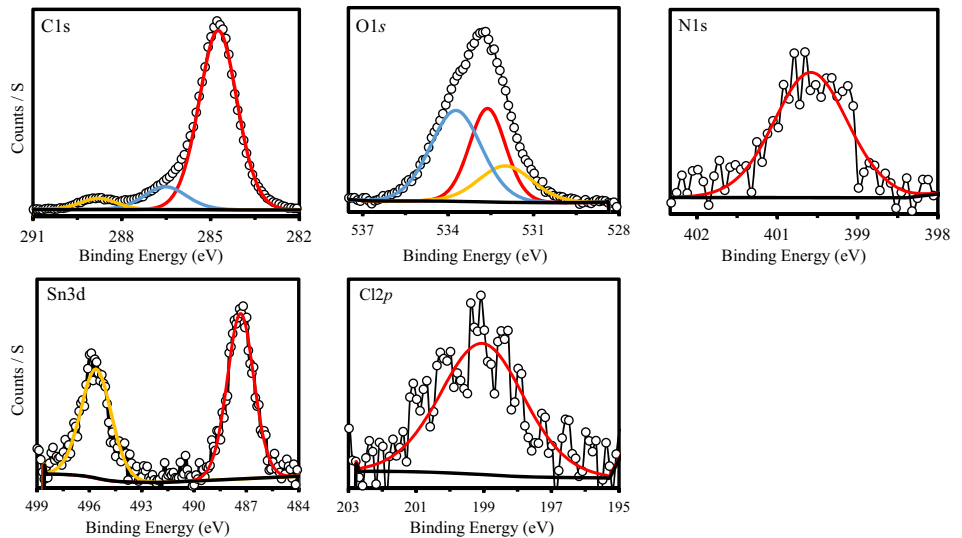

Figure 4 XPS survey scan spectra of polymer nanocomposite **a** fitting high-resolution results of C1s/O1s/N1s/Cl2p/Sn3d.

interstitial polymer sites. Surprisingly, the absence of Ag signals in the survey spectrum is expected as the XPS is a surface analysis within 1–3 nm, i.e., Ag is doped in the film core, while the Cl 2p signal appears at 199.04 eV, confirming the formation of AgCl, which agreed with the obtained XRD results. The C

1 s spectrum is deconvoluted into three peaks with binding energies (BE) values of 284.7, 286.5, and 288.8 eV corresponding to C–C/C-H, C–OH/C–N, and C = O functional groups, respectively [36, 40]. The O 1 s peak also shows three peaks at BE values of 531.5, 532.1, and 533.3 eV corresponding to Sn–O/lattice oxygen, C = O/C–OH/H_2O, and C–O–C, respectively [36]. The N 1 s appears at 399.9 eV corresponding to C–N. The Sn 3d spectrum is identified by two peaks around 487.24 eV (Sn $3d_{5/2}$) and 495.61 eV (Sn $3d_{3/2}$)[40, 41]. The BE of the Sn $3d_{5/2}$ peak at 487.24 eV indicates the presence of SnO or SnO_2 since their BEs are similar; this is likely due to partial reduction of Sn^{4+} [42], consistent with Raman measurements.

FTIR analysis

FTIR was employed to analyze the chemical bonding, composition, and evaluate the chemical stability of the prepared nanocomposite polymer (Figure SI4). A strong and broad band appears around 3235 cm^{-1}: this is generally attributed to the contributions of stretching vibration of C–OH group and amine group of PVP monomer moiety and hydrogen bonds of the crosslinking polymer, in addition the possible vibrations of Sn-OH mode [15, 43]. Another characteristic peak of amine, i.e., C–N stretching modes appeared at 1289 cm^{-1} [43]. The absorption band assignable to C = O stretching vibration is observed at 1647 cm^{-1}, which indicated the presence of PVP [28]. The absorption peak at 1066 and 1032 cm^{-1} is generally assigned to the stretching vibrations of secondary–OH group and C–O stretching and –OH bending vibrations, respectively [43]. The band at 842 cm^{-1} is specified to Sn–O stretching vibration of SnO_2 [44]. It is notable that the FTIR spectrum of the polymer nanocomposite, after gamma radiation exposure, is very similar to the raw material spectrum before radiation exposure. This result emphasizes that the proposed polymer nanocomposite has a radiation stability against γ-radiation at different energies.

Chemical stability investigation

The chemical stability of the proposed polymer nanocomposite was tested and evaluated under different conditions. The weight loss was found to be about 4–8% compared to the raw polymer nanocomposite under the same conditions, and the highest weight loss was observed in HNO_3 solutions. This may be due to the solubility of the unreacted starting polymer due to the PVA/PVP ratio, dissolving of the SnO_2, or the AgCl of the surface. Moreover, the chemical composition stability of the material was analyzed by FTIR spectroscopy. After γ-ray shielding experiments (FTIR section), it turns out that the proposed polymer nanocomposite remains remarkably stable and durable.

Thermal analysis

The thermogravimetric analyses (TGA), differential thermal analysis (DTA), and differential scanning calorimetry (DSC) profiles are shown in Fig. 5. TGA degradation profile follows a simple degradation profile as follows: (a) the first step (up to 125 °C) corresponds to the release of structural water content (represents a weight loss about 25%, w/w), (b) the second step (in the range 125–390 °C) involves a weight loss of about 16.5% (total wt%: 53–56%); this step corresponds to the degradation of amine, hydroxyl, and ether moieties of the organic polymer composition [36], (c) the third step (from 390-to-424 °C) is followed by a weight loss close to 9–10% (total wt%: ≈66%): corresponding to the depolymerization and decomposition of the PVP-five-membered ring, (d) the fourth step (from 424 to 515 °C) corresponds to the sharp weight decrease (with the highest rate of weight loss close to 515 °C, given by the TDG, which represents a weight loss of 24%), and (e) the final plateau (from 515 to 880 °C) that corresponds to the complete combustion of the
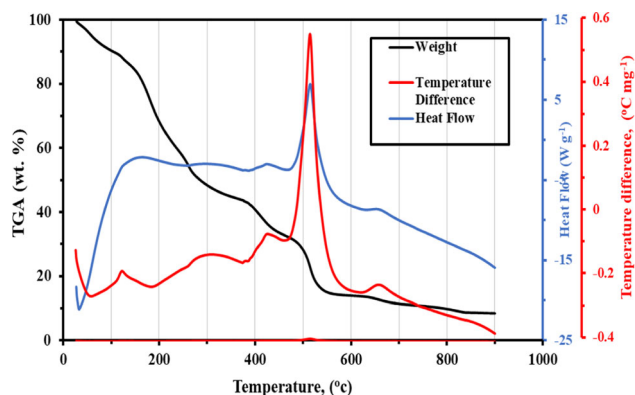

Figure 5 Thermal analysis (TGA, DTA, and DSC) of the polymer nanocomposite.

organic residue which represents a weight loss of 7%. (The total wt%: $\approx 91\%$).

For the DTA curve of the nanocomposite polymer, a strong exothermic peak is observed at about 515.1 °C that could be attributed to the conversion of $Sn(OH)_4$ into SnO_2 (which includes dehydroxylation and phase transition, TGA panel), consistently with DSC panel [45]. The characteristic endothermic peaks are appeared at around 123.3 °C, 424.1 °C, 515.1 °C, and 659.4 °C due to the releasing of absorbed water, the degradation of function groups of organic polymer and depolymerization and decomposition, and the dehydration and phase conversion and complete combustion of the organic residue, respectively (DSC panel). The strong DSC peak observed at 515.1 °C for tin hydroxide corresponds to the transition for the formation of $Sn(OH)_4$ consistently with Raman and FTIR measurements. It is not possible detecting a strong peak; the heat release continuously decreases with absolute values (5 to $-$ 25 W g^{-1}). The thermal profile also confirms the stability of the bonded chloride in AgCl; indeed, it was not possible detecting any peak assigned to the release of chloride/chlorine even at high temperatures [45].

Radiation shielding studies

The interaction of gamma radiation as an electromagnetic wave with matter occurs through different mechanisms known as; (i) photoelectric effect, (ii) Compton scattering, (iii) Rayleigh scattering, and (iv) pair production. One of the most important issues is understanding of the radiation manner as interaction with matter and transfers its energy. The transfer of radiation energy to matter is occurred by two processes: the first one is the ionization process, which occurs by elimination of an electron from an atom producing a new atom with a net positive charge, and the second one is the excitation, in this process the incident radiation upon the mater releases energy elevating one external electron to a higher state of energy. Meanwhile, through the radiolysis process of polymers, several reactions can cause increase or decrease in the polymer molecular weight as a result of the cross-linking and chain scission that can be occurred synchronously as an effect of radiation [2, 46]. So, the preparation of the polymer nanocomposite is by adding HF, giving PVA/PVP/AgCl/SnO$_2$:F, which plays a significant role in encouraging γ-ray absorption. The electronegativity of the F, N,

and O atoms can produce dipoles inside Sn, Ag, and the functional groups of the polymer. The process of depolarization takes place as an effect of interaction with incident γ-ray, which successively enhances the shielding absorption properties [2].

The concept of γ-radiation protection using shielding is essential for radiation protection programs in order to reduce the exposure of personnel to ionizing radiation. As a new domain to utilize polymer nanocomposite in the radiation attenuation process, more investigation is required to understand the basic principles of γ-ray interactions with the polymer nanocomposite. The basic processes of γ-rays interaction with matter for perfect γ-radiation absorption, mainly occurs as photoelectric effect and pair production processes, whereas the other remained processes may be produced as partial degradation energy. The transmitted intensity of photons was determined at different energies 662, 1173, 1332 keV (Fig. 6) to calculate the linear attenuation coefficient.

Linear and mass attenuation coefficients of the polymer nanocomposite were gained from the transmission factor curves by applying Lambert law (Section I, see Supporting Information Section) with an excellent correlation coefficient (R^2). Figure 7 demonstrates that the attenuation coefficient values of γ-radiation for the proposed polymer nanocomposite were 0.1047 for ^{137}Cs and 0.0773, 0.0707 for ^{60}Co. The variation between theoretical results that have been acquired by the XCOM program (Fig. 7) and the experimental data of the mass attenuation coefficient for the fabricated polymer nanocomposite
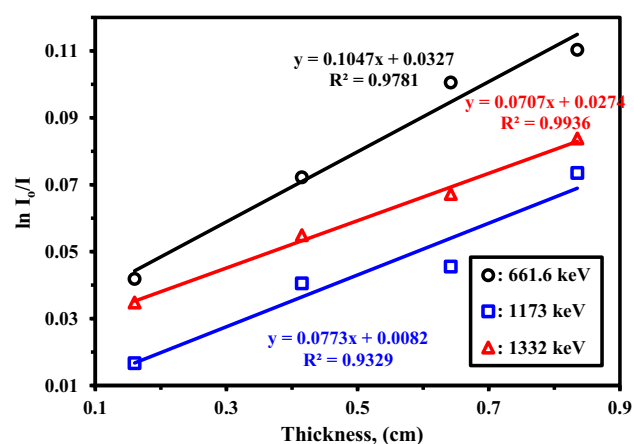

Figure 6 Plot of $\ln(I_0/I)$ *vs.* attenuator polymer nanocomposite thickness at different photon energy.
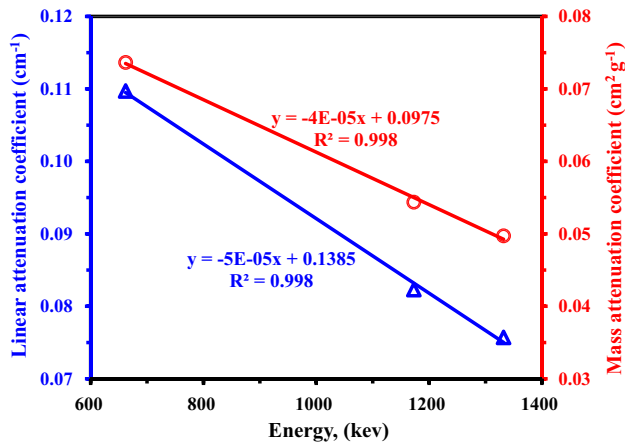
Figure 7 Linear and mass attenuation coefficients *vs* polymer nanocomposite energy.

that was exposed to different photon energies is demonstrated in Table 1. Also, Table 1 presents a comparison between the acquired data with other available previous works data. In general, the increasing density of the protective material will lead to an increase in gamma-ray attenuation. Subsequently, the XCOM calculated data values are relatively higher comparing with the experimental results that may be due to the XCOM code and the model itself (physical and/ or mathematical models),

linear and mass attenuation coefficients uncertainties of the fabricated polymer nanocomposite for the studied γ-rays point sources, incorrect modeling of energy source and actual geometry finally error in the polymer nanocomposite compositions, the environment conditions (humidity, pressure, and temperature), and physical quantities measurement errors (as; dimensions, densities, elemental composition of materials, intensity of sources). The calculated theoretical value of the mass attenuation coefficient for lead element was $0.1101 cm^2/g$. Through comparison, the mass attenuation coefficient values of the fabricated polymer nanocomposite represented 75.5% of the lead value at photon energy 662 keV, 56.8% at 1173 keV, and finally 53.1% at 1332 keV. Generally, the higher coefficients of the polymer nanocomposite predictors of a better attenuation properties, which achieved in the studied fabricated polymer nanocomposite, may be ascribed to a higher ratio of the surface (larger photon interaction cross section) to its volume and improved dispersal in the polymer matrix (see Fig. 8).

Another way for assessment of shielding effectiveness of the investigated polymer nanocomposite is to calculate the half value layer thicknesses that attenuate one half (50% attenuation) of γ-ray original

Table 1 Comparison of theoretically (XCOM) and experimental mass attenuation coefficient (μ_m) with various polymeric materials

| Energy	Theoretical μ_m (cm^2 g^{-1})			Experimental μ_m (cm^2 g^{-1})			References
	661.6 keV	1173 keV	1332 keV	661.6 keV	1173 keV	1332 keV	
Polymeric materials							[11]
Polyethylene (PE)	0.0911	0.0655	0.0603	0.112	0.0540	0.0560	
Polycarbonate (PC)	0.0853	0.0614	0.0565	–	–	–	
Polyethyleneterephthalate (PET)	0.0831	0.0598	0.0551	–	–	–	
Polystyrene (PS)	0.0858	0.0618	0.0569	0.0827	0.0744	0.0505	
Polyvinylalcohol (PVA)	0.0870	0.0626	0.0576	–	–	–	
Polyvinylchloride (PVC)	0.0822	0.0588	0.0541	–	–	–	
Polyvinylpyrrolidone (PVP)	0.0862	0.0620	0.0571	–	–	–	
Polypropylene (PP)	0.0910	0.0655	0.0603	0.0720	0.0540	0.0580	
PVA/WO$_3$	–	–	–	0.0599	0.0432	0.0408	[21]
Polyboron	–	–	–	0.0867	0.0660	0.0618	[6]
Ordinary concrete	–	–	–	0.0775	0.0588	0.0551	
Borated polyethylene	–	–	–	0.0821	0.0624	0.0584	
Polymethylmethacrylate (PMMA)	0.0862	0.0620	0.0571	0.0660	0.0490	0.0530	[7]
				0.0867	0.0661	0.0613	
Polymer nanocomposite (PVA/PVP/HF/AgCl/ SnO$_2$:F)	0.0824	0.0626	0.0587	0.0736	0.0544	0.0497	This work
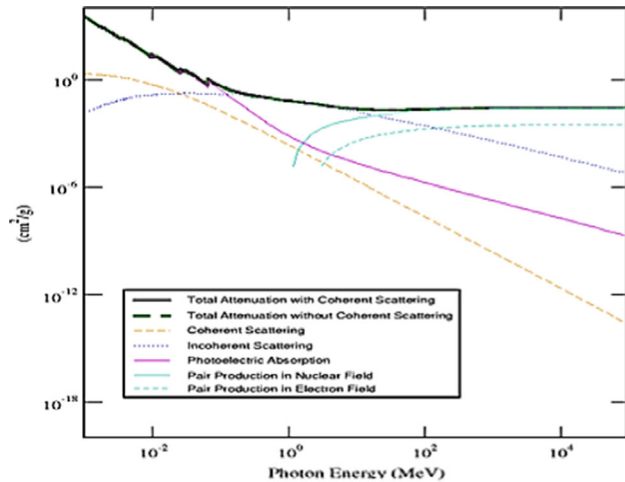
Figure 8 XCOM Mass attenuation coefficient, μ_m (cm^2 g^{-1}), *vs* incident photon energy of polymer nanocomposite for total and partial interactions (https://physics.nist.gov/PhysRefData/Xcom/html/xcom1.html).
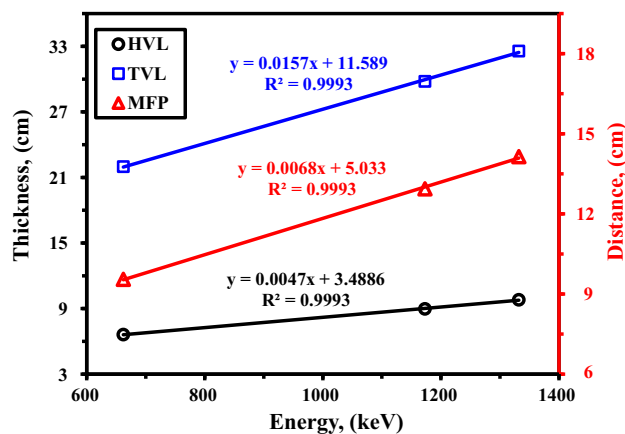

Figure 9 HVL, TVL, and MFP *vs* energy for polymer nanocomposite.

intensity. However, TVL describes the thickness of the polymer nanocomposite as a shielding material that can minimize the radiation effects by a factor of one tenth of initial level (90% attenuation) [7, 9]. The shielding calculations exactly depend upon the concepts of HVL and TVL, which are more helpful to rapid approximate calculations [6, 13]. Whereas HVL and TVL values are known, the penetration through other thicknesses can be easily determined. The variance of HVL and TVL values of the selected polymer nanocomposite with incident photon energy is shown in (Fig. 9). It was observed that the HVL values were increased slightly by increasing the energy, whereas the essential thickness of the

polymer nanocomposite to attenuate the intensity of γ-ray to 50% than initial is 6.6, 8.9 and 9.8 cm for γ-ray energies, 662, 1173, and 1332 keV, respectively. Description of the increased HVL values at higher energy levels may be ascribed to the increased γ-ray energy, which is the required thickness to disperse the fallen radiation into half. The evaluated TVL of the polymer nanocomposite at the previously mentioned energy source is demonstrated in Fig. 9.

Moreover, the mean free path is expressing an average of two successive traveled γ-beams distance (Fig. 9). The mean free path was computed by inversion of the linear attenuation coefficient value (μ). Thus, a lower value of HVL, as well as MFP, indicates more effective protection. It is found that the lower the HVL and TVL values, the higher the radiation shielding material in terms of the thickness requirements.

Comparison of the fabricated polymer nanocomposite with other materials

The shielding properties of different polymeric materials to γ-radiation were compared to each other theoretically and experimentally. The compared parameters are mass attenuation coefficient (μ_m) in cm^2 g^{-1} (Table 1) and the calculated data of HVL and TVL in cm, with respect to the fabricated polymer nanocomposite (PVA/PVP/Ag/SnO$_2$:F) (Table SI2). Since the experimental conditions are not identical (e.g., chemical composition, thickness, mass ratios, and filling agent), a direct comparison is not easy. The experimental μ_m results show that the fabricated nanocomposite (PVA/PVP/HF/Ag/SnO$_2$:F) has a comparable shielding properties to conventional polymers and polymer composites, e.g., polypropylene (PP) [11], polymethylmethacrylate (PMMA) [7], and polymer composite (PVA/WO$_3$) [21], while some other polymers, e.g., polystyrene (PS), high dense polyethylene (PE) [11], and polyboron [6], show slightly higher efficiency compared to our polymer nanocomposite. However, (PVA/PVP/Ag/SnO$_2$:F) polymer nanocomposite has comparable results in terms of four parameters (theoretical and experimental μ_m values, HVL and TVL) than most of the reported materials (though not exactly under the same experimental conditions).

Conclusion

A new polymer nanocomposite of polyvinyl alcohol/ polyvinyl pyrrolidone in the presence of HF (PVA/ PVP film containing $AgCl/SnO_2$ nanocomposite) via a one-pot synthesis reaction has been successfully synthesized. XRD, SEM–EDX analysis including mapping, Raman analysis, XPS, TEM, and thermal analysis were used to characterize the synthesized nanocomposite and confirm the synthesis route. XRD confirmed the existence of $Ag^0/AgCl$ nanoparticles with in a crystalline nature with Ag face-centered cubic structure. The TEM images explained the AgCl and SnO_2 NPs actual size and the morphology as well. The average particle size was found to be 11.4 ± 2.2 nm for AgCl NPs showing a narrow size distribution, while SnO_2 nano-size was 26 ± 7 nm with a broad size distribution, according to the obtained histogram with a regular spherical dot structure. The SEM images revealed that the polymer surface is soft and has smooth planar structure with no porosity. XPS and Raman analysis confirmed the presence of SnO_x (hydrous/oxide form) with two different oxidation states. Interestingly, the absence of Ag and detection of Cl on the surface (1–3 nm in depth) in the XPS confirm that the AgCl was doped inside the polymer film. FTIR analysis for the synthesized polymer nanocomposite before and after radiation exposure reveals its chemical stability against the radiation. This was further approved by the chemical leachability investigation that reveals the durability under several reagents conditions. The synthesized polymer nanocomposite was applied and tested for γ-ray attenuation. The attenuation capacity was investigated in terms of linear and mass attenuation coefficients (μ) and (μ_m), respectively, at a low and high energies (^{137}Cs and ^{60}Co). The experimental results were compared with XCOM program results, and it was concluded that the fabricated nanocomposite polymer has shielding properties perfectly adequate for γ-ray. Finally, HVL, TVL, and MFP parameters provide that the essential thickness of the fabricated polymer nanocomposite to reduce the γ-ray intensity to 50% is 6.6, 8.9 and 9.8 cm for 662, 1173, and 1332 eV, respectively.

Declarations

Conflict of interest The authors declare no conflict of interest.

Supplementary Information: The online version contains supplementary material available at http s://doi.org/10.1007/s10853-022-07213-9.

References

[1] Ramdani N (2020) Micro and nanostrued composite materials for neutron shielding applications: Introduction to neutron shielding, 1st edn. Elsevier, Amsterdam

[2] Bora PJ, Anil AG, Ramamurthy PC, Tan DQ (2020) MXene interlayered crosslinked conducting polymer film for highly specific absorption and electromagnetic interference shielding. Mater Adv 1:177–183. https://doi.org/10.1039/D0MA00005A

[3] Nambiar S, Yeow JTW (2012) Polymer-composite materials for radiation protection. ACS Appl Mater Interfaces 4:5717–5726. https://doi.org/10.1021/am300783d

[4] Akman F, Ozkan I, Kaçal MR, Polat H, Issa SAM, Tekin HO, Agar O (2021) Shielding features, to non-ionizing and ionizing photons, of FeCr-based composites. Appl Radiat Isot 167:109470. https://doi.org/10.1016/j.apradiso.2020.109470

[5] Paul S (2019) Biomedical engineering and its applications in healthcare: Nanostructured Materials and Their Biomedical Application. Springer Nature Singapore Pte Ltd, Singapore, pp 205–227

[6] Biswas R, Sahadath H, Mollah AS, Huq MF (2016) Calculation of gamma-ray attenuation parameters for locally developed shielding material: polyboron. J Radiat Res Appl Sci 9:26–34. https://doi.org/10.1016/j.jrras.2015.08.005

[7] Singh VP, Shirmardi SP, Medhat ME, Badiger NM (2015) Determination of mass attenuation coefficient for some polymers using Monte Carlo simulation. Vacuum 119:284–288. https://doi.org/10.1016/j.vacuum.2015.06.006

[8] Ud-Din Khan S, Ud-Din Khan S, Almutairi Z, Haider S, Ali SM (2020) Development of theoretical-computational model for radiation shielding. J Radiat Res Appl Sci 13:606–615. https://doi.org/10.1080/16878507.2020.1812798

[9] Bayoumi EE, Abd El-Magied MO, Elshehy EA, Atia BM, Mahmoud KA, Khalil LH, Mohamed AA (2022) Lead–bismuth tungstate composite as a protective barrier against gamma rays. Mater Chem Phys 275:125262. https://doi.org/10.1016/j.matchemphys.2021.125262

[10] Mann HS, Brar GS, Mudahar GS (2016) Gamma-ray shielding effectiveness of novel light-weight clay-flyash bricks. Radiat Phys Chem 127:97–101. https://doi.org/10.1016/j.radphyschem.2016.06.013

[11] Mirji R, Lobo B (2017) Computation of the mass attenuation coefficient of polymeric materials at specific gamma photon energies. Radiat Phys Chem 135:32–44. https://doi.org/10.1016/j.radphyschem.2017.03.001

[12] Saim A, Tebboune A, Berkok H, Belameiri N, Belbachir AH (2014) Linear and mass attenuation coefficient for CdTe compound for X-rays from 10 to 100keV energy range in different phases. J Alloy Compd 602:261–264. https://doi.org/10.1016/j.jallcom.2014.03.012

[13] Buyuk B, Tugrul AB (2014) Comparison of lead and WC-Co materials against gamma irradiation. Acta Phys Pol A 125:423–425. https://doi.org/10.12693/APhysPolA.125.423

[14] Luković J, Babić B, Bučevac D, Prekajski M, Pantić J, Baščarević Z, Matović B (2015) Synthesis and characterization of tungsten carbide fine powders. Ceram Int 41:1271–1277. https://doi.org/10.1016/j.ceramint.2014.09.057

[15] Galhoum AA, Atia AA, Mahfouz MG, Abdel-Rehem ST, Gomaa NA, Vincent T, Guibal E (2015) Dy(III) recovery from dilute solutions using magnetic-chitosan nano-based particles grafted with amino acids. J Mater Sci 50:2832–2848. https://doi.org/10.1007/s10853-015-8845-z

[16] More CV, Alsayed Z, Badawi MS, Thabet AA, Pawar PP (2021) Polymeric composite materials for radiation shielding: a review. Environ Chem Lett 19:2057–2090. https://doi.org/10.1007/s10311-021-01189-9

[17] Kiani MA, Ahmadi SJ, Outokesh M, Adeli R, Kiani H (2019) Study on physico-mechanical and gamma-ray shielding characteristics of new ternary nanocomposites. Appl Radiat Isot 143:141–148. https://doi.org/10.1016/j.apradiso.2018.10.006

[18] Kaçal MR, Akman F, Sayyed MI, Akman F (2019) Evaluation of gamma-ray and neutron attenuation properties of some polymers. Nucl Eng Technol 51:818–824. https://doi.org/10.1016/j.net.2018.11.011

[19] Saini P, Choudhary V, Singh BP, Mathur RB, Dhawan SK (2011) Enhanced microwave absorption behavior of polyaniline-CNT/polystyrene blend in 12.4–18.0GHz range. Synth Metals 161:1522–1526. https://doi.org/10.1016/j.synthmet.2011.04.033

[20] Bryning MB, Islam MF, Kikkawa JM, Yodh AG (2005) Very low conductivity threshold in bulk isotropic single-walled carbon nanotube-epoxy composites. Adv Mater 17:1186–1191. https://doi.org/10.1002/adma.200401649

[21] Kazemi F, Malekie S, Hosseini MA (2019) Study on the shielding properties of a novel polyvinyl alcohol (PVA)/WO(3) composite, against gamma rays, using the MCNPX code. J Biomed Phys Eng 9:465–472. https://doi.org/10.31661/jbpe.v0i0.1114

[22] Eid M, El-Arnaouty MB, Salah M, Soliman E-S, Hegazy E-SA (2012) Radiation synthesis and characterization of poly(vinyl alcohol)/poly(N-vinyl-2-pyrrolidone) based hydrogels containing silver nanoparticles. J Polym Res 19:9835. https://doi.org/10.1007/s10965-012-9835-3

[23] Qiao J, Fu J, Lin R, Ma J, Liu J (2010) Alkaline solid polymer electrolyte membranes based on structurally modified PVA/PVP with improved alkali stability. Polymer

51:4850–4859. https://doi.org/10.1016/j.polymer.2010.08.018

[24] Bai J, Ma X, Yan H, Zhu J, Wang K, Wang J (2020) A novel functional porous organic polymer for the removal of uranium from wastewater. Microporous Mesoporous Mater 306:110441. https://doi.org/10.1016/j.micromeso.2020.110441

[25] Karan R, Manna P, Maiti PK, Das K (2020) Influence of selenium dioxide (SeO2) on properties of bioglass in SiO2-Na2O-CaO-P2O5 system. J Aust Ceram Soc 56:1135–1145. https://doi.org/10.1007/s41779-020-00459-z

[26] Lebrun L, Follain N, Metayer M (2004) Elaboration of a new anion-exchange membrane with semi-interpenetrating polymer networks and characterisation. Electrochim Acta 50:985–993. https://doi.org/10.1016/j.electacta.2004.07.040

[27] Aslam M, Kalyar MA, Raza ZA (2018) Polyvinyl alcohol: a review of research status and use of polyvinyl alcohol based nanocomposites. Polym Eng Sci 58:2119–2132. https://doi.org/10.1002/pen.24855

[28] Zhang Q, Liu F, Li L, Pan G, Shang S (2011) Magnetic ionic liquid-assisted synthesis of polyaniline/AgCl nanocomposites by interface polymerization. J Nanopart Res 13:415–421. https://doi.org/10.1007/s11051-010-0070-8

[29] Pearson RG (1966) Acids and bases. Science 151:172–177. https://doi.org/10.1126/science.151.3707.172

[30] Fajans K (1923) Struktur und Deformation der Elektronenhüllen in ihrer Bedeutung für die chemischen und optischen Eigenschaften anorganischer Verbindungen. Naturwissenschaften 11:165–172. https://doi.org/10.1007/BF01552365

[31] Tyrra W (2002) Silver(I) fluoride and related compounds in chemical synthesis. Heteroat Chem 13:561–566. https://doi.org/10.1002/hc.10102

[32] Wang J, Liu S, Cao X, Wang Z, Guo Y, Li X, Liu C, Jiang W, Wang H, Wang N et al (2019) One-pot synthesis and gas sensitivity of SnO2 nanoparticles prepared using two Sn salts of SnCl4·5H2O and SnCl2·2H2O. Appl Phys A 126:44. https://doi.org/10.1007/s00339-019-3230-4

[33] Ikhmayies SJ (2019) Optical parameters of nanocrystalline SnO2: F thin films prepared by the spray pyrolysis method. JOM 71:1507–1512. https://doi.org/10.1007/s11837-019-03388-w

[34] Ikhmayies SJ (2019) Spray deposited thin films of SnO2: F/CdS: in bilayers produced using different fluorine sources: NH4F and HF. J Energy Syst 3:111–122. https://doi.org/10.30521/jes.605085

[35] Ibarguen CA, Mosquera A, Parra R, Castro MS, Rodríguez-Páez JE (2007) Synthesis of SnO2 nanoparticles through the controlled precipitation route. Mater Chem Phys 101:433–440. https://doi.org/10.1016/j.matchemphys.2006.08.003

[36] Morshedy AS, Galhoum AA, Aleem A, Abdel Aleem H, Shehab El-din MT, Okaba DM, Mostafa MS, Mira HI, Yang Z, El-Sayed IET- (2021) Functionalized aminophosphonate chitosan-magnetic nanocomposites for Cd(II) removal from aqueous solutions: performance and mechanisms of sorption. Appl Surf Sci 561:150069. https://doi.org/10.1016/j.apsusc.2021.150069

[37] Assis M, Groppo Filho FC, Pimentel DS, Robeldo T, Gouveia AF, Castro TFD, Fukushima HCS, de Foggi CC, da Costa JPC, Borra RC et al (2020) Ag nanoparticles/AgX (X=Cl, Br and I) composites with enhanced photocatalytic activity and low toxicological effects. ChemistrySelect 5:4655–4673. https://doi.org/10.1002/slct.202000502

[38] Akyil C, Akdas G, Afsin P, Ürgen M (2019) Freestanding SnO2 films produced with anodic polarization in acidic media containing colloidal tin hydroxides. Mater Chem Phys 221:263–271. https://doi.org/10.1016/j.matchemphys.2018.09.062

[39] Morshedy AS, Tawfik SM, Hashem KM, Abd El-Aty DM, Galhoum AA, Mostafa MS, Guibal E (2021) The production of clean diesel fuel by facile sun light photocatalytic desulfurization process using Cd-based diacetate as a novel liquid photocatalyst. J Cleaner Prod 279:123629. https://doi.org/10.1016/j.jclepro.2020.123629

[40] Bhangare B, Ramgir NS, Jagtap S, Debnath AK, Muthe KP, Terashima C, Aswal DK, Gosavi SW, Fujishima A (2019) XPS and Kelvin probe studies of SnO2/RGO nanohybrids based NO2 sensors. Appl Surf Sci 487:918–929. https://doi.org/10.1016/j.apsusc.2019.05.176

[41] Kwoka M, Lyson-Sypien B, Kulis A, Zappa D, Comini E (2018) Surface properties of SnO2 nanowires deposited on Si substrate covered by Au catalyst studies by XPS, TDS and SEM. Nanomaterials 8:738. https://doi.org/10.3390/nano8090738

[42] Moulder JF, Stickle WF, Sobol PE, Bomben KD (1978) Handbook of x ray photoelectron spectroscopy In: CD Wanger, WM Riggs, LE Davis, JF Moulder and GE Muilenberg Perkin Elmer Corp. (eds) Physical Electronics Division, Eden Prairie, Minnesota, USA, 1979. 190 pp. $195. 3

[43] Coates J (2000) Interpretation of infrared spectra: a practical approach. Encyclopedia of analytical chemistry. Wiley, Chochester, pp 10815–10837

[44] Chen F, Yang Q, Niu C, Li X, Zhang C, Zeng G (2015) Plasmonic photocatalyst Ag@AgCl/ZnSn(OH)6: synthesis, characterization and enhanced visible-light photocatalytic activity in the decomposition of dyes and phenol. RSC Adv 5:63152–63164. https://doi.org/10.1039/C5RA10480G

[45] Mostafa MS, El Naga AOA, Galhoum AA, Guibal E, Morshedy AS (2019) A new route for the synthesis of self-acidified and granulated mesoporous alumina catalyst with superior Lewis acidity and its application in cumene conversion. J Mater Sci 54:5424–5444. https://doi.org/10.1007/s10853-018-03270-1

[46] Manjunatha HC (2017) A study of gamma attenuation parameters in poly methyl methacrylate and Kapton. Radiat Phys Chem 137:254–259. https://doi.org/10.1016/j.radphyschem.2016.01.024

Publisher's Note Springer Nature remains neutral with regard to jurisdictional claims in published maps and institutional affiliations.